Structural, dielectric, and magnetic properties of $LaCo_{0.2}Mn_{0.8}O_3$ and La_2CoMnO_6 perovskite materials

N. M. Yousif [1] · N. Makram[2] · L. A. Wahab[1]

Abstract

Herein report, we aim to study the structural, dielectric, and magnetic properties for multifunctional perovskite materials $LaCo_{0.2}Mn_{0.8}O_3$ and La_2CoMnO_6 nanoparticles, which were synthesized by a modified sol–gel route. Citric acid was processed as the chelating agent; gelation slurry formed by irradiation process which exposed to a total gamma radiation dose of 25 kGy at a dose rate of ~1.2 Gy/h to obtain more stability and high purity multifunctional perovskite materials. XRD notarizes the genesis of one pure phase orthorhombic perovskite structure. A full agreement between the particle sizes was investigated by HRTEM and the XRD data was observed. Raman spectra result assigned to the antisymmetric stretching mode and symmetric stretching mode of the (Co/Mn) O_6 octahedra, which related to lattice distortions. The as-prepared perovskite materials exhibit ferromagnetic nature with different values of magnetization. Electron Spin Resonance (ESR) measurements are also carried out in the LCMO multifunctional nanoparticle systems, which suggests the occurrence of Jahn–Teller glass analogous to the spin-glass behavior. The complex impedance displayed high impacts on the electrical properties. The high value of dielectric constant for LCMO prepared nanoparticle systems may be used in electric tunable devices.

✉ N. M. Yousif
   yousif_nashwa@yahoo.com

1   Solid-State and Accelerators Department, National Center for Radiation Research & Technology (NCRRT), Egyptian Atomic Energy Authority (EAEA), Cairo, Egypt

2   Nano-Materials Laboratory, Physics Department, Faculty of Science, Al-Azhar University, Cairo, Egypt

Graphical Abstract

$$(La3^+, Co^{2+}, Mn^{2+})(NO^3)_{5-6-x}(Cit^3) \rightarrow LaCoMnO_3 + (5-6x) NO_2 + 12xCo_2 + 5xH_2O + (1-11.5x) O_2$$
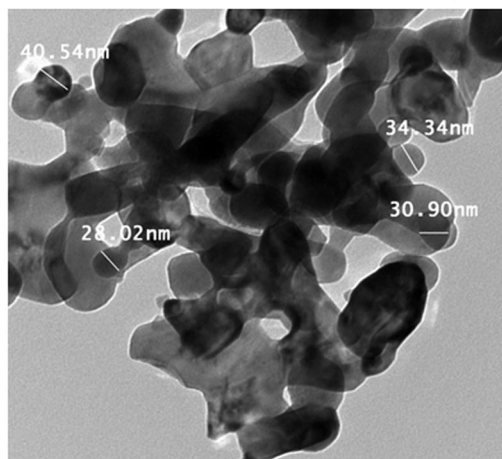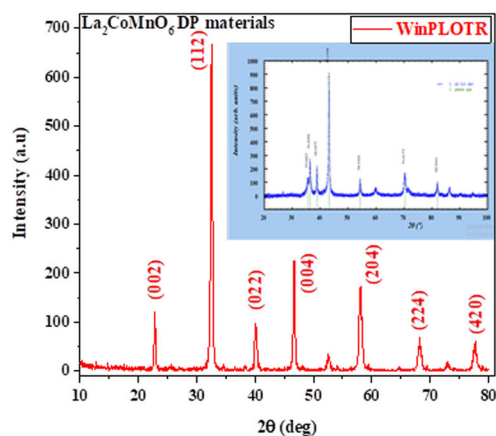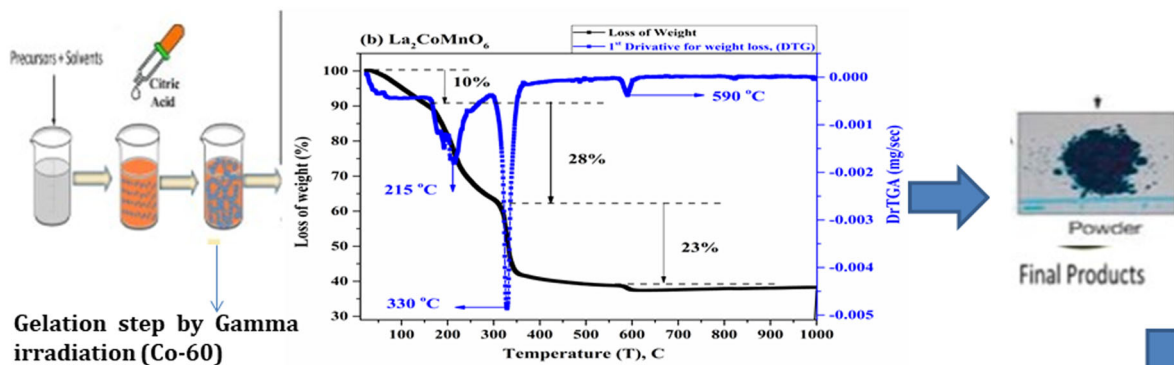
Keywords Perovskite and double perovskite · Modified sol–gel route by gamma radiation · Magnetic properties · Dielectric properties

Highlights

- Novel modified sol-gel route by gamma radiation used to synthesis more stability and high purity multifunctional perovskite materials ($LaCo_{0.2}Mn_{0.8}O_3$, and La_2CoMnO_6).
- These multifunctional materials have orthorhombic structure lattices.
- LCMO multifunctional nanoparticle systems have a spin-glass behavior.
- The high value of dielectric constant for LCMO nanoparticle multifunctional materials is promising in electric tunable devices.

Abbreviations

DP	(Double Perovskite)
LCMO	(Lanthanum Cobalt Manganese oxide)
LNMO	(Lanthanum Nickel Manganese oxide)
FM	(Ferromagnetic)
TMs	(transition metals)
DC	conductivity (Direct Current conductivity)
FC	(Field Cooling)
ZFC	(Zero Field Cooling)
GP	(Griffiths Phase)
TC	(magnetic transition temperature or Curie Temperature)

1 Introduction

Multifunctional materials with perovskite category structures possess expanded physical properties such as dielectric, ferroelectric, ferro-/antiferromagnetic, and electronic/ionic conductions to use for the electric prospective applications. Such types from these materials are used in solar cells, electric tunable devices, biomolecular, and gas sensing technologies, and spintronics and magneto-electric devices [1].

In the AMO_3 perovskite, A = rare-earth (where, A = La, Nd, Sm, Gd, and Pr), M = transition metal ions (like, Mn,

Co, Fe, etc.), while A$_2$MM'O$_6$ double perovskite (A = rare-earth or alkaline earth ions; M and M' = 3d transition metal ions) are a type of perovskites which have represented noteworthy attention [2–6]. The characteristic property of an ordered rock-salt is the arrangement of corner-sharing MO$_6$ and M'$_6$ units in the crystal structure. As a result of alternative composition in structure for double perovskite materials, a vast diversity of physical properties in DPs (*Double Perovskite*) is exhibited [7]. Strong conjunction between the magnetic and dielectric properties in some multifunctional double perovskite systems with the cohabitation of insulating and ferromagnetic properties has acquired significant research interest. Lanthanum-based perovskite-type oxides (such as LCMO (*Lanthanum Cobalt Manganese oxide*), and LNMO (*Lanthanum Nickel Manganese oxide*), etc.) are fascinating materials due to having good optical, electrical, and magnetic properties. The applications of these materials (e.g. gas sensors, catalysts, thermoelectric material, electrode materials in solid oxide fuel cells, etc.) lead to a wide range of interest in their synthesis and structural analysis [8–10]. Double perovskite La$_2$CoMnO$_6$ has received enormous research interest because of its reasonably large magneto-capacitance and magneto-resistance. Counting on the method of synthesis, optimum performance, and effective properties of well-defined microstructures are suitable [11]. The Spectroscopic studies [12] on LaMnCoO$_3$ compounds indicate that a mixture of Mn^{3+} and Mn^{4+} is present in this series, and therefore a double-exchange mechanism is required to account for the ferromagnetism of these compounds. Normally, in a disordered double perovskite series, each of the B-site cations is in the 3$^+$ oxidation state. However, in the ordered phase, the ferromagnetic behavior appears because of the super interchange interaction between the cations Co^{2+} and Mn^{4+} [13, 14]. Therefore, the debate subsists around the electronic state of the transition metals (TMs) in this family of compounds.

Numerous techniques have been advanced to focus on the problem of perovskite purity; the most frequently used of these is the sol–gel citrate (SGC) method. The complexing agent used in SGC is citric acid. This method prepares it possible to obtain a high surface area, but it has the weakness of rather rapid sintering depending on the temperature [15]. Nevertheless, our novel method presented good advantages such as lower temperature compared to the solid-state reactions, better homogeneity, improved reactivity, and new compositions, and better control of stoichiometry, particle size, and purity. Consequently, this novel method has opened new directions for molecular architecture in the synthesis of perovskites.

This paper aims to novel synthesized by using gamma irradiation to obtain a gel product instead of heat treatment for LCMO multifunctional materials. I am reporting in this current article for the first time that, the synthesis of LaCo$_{0.2}$Mn$_{0.8}$O$_3$and La$_2$CoMnO$_6$ perovskite materials by modified sol–gel route (citrate-gel method); Gelation step was carried out by gamma radiation in the Cobalt-60 gamma cell source (made in Russia) installed at the National Centre for Radiation Research and Technology, Cairo, Egypt (dose rate 1.2 Gy/h). This method of preparation is environmentally friendly, low cost, high stability, and low toxicity over large-scale commercial applications. I am also describing their electric, dielectric, and magnetic properties to compare with the difference between perovskite and double perovskite materials in properties.

2 Experimental technique

2.1 Materials

LaCo$_{0.2}$Mn$_{0.8}$O$_3$ and La$_2$CoMnO$_6$ nanoparticles were synthesized by a modified sol–gel route (citrate-gel method) from their nitrate precursors. Lanthanum Nitrate, Cobalt Nitrate, Manganese (II) acetate tetrahydrate, Citric Acid acts as fuel to speed the reaction, and Nitric Acid was taken up from Alfa Aesar with purity (99.99%). Gelation by gamma radiation was done in the Cobalt-60 gamma cell source (made in Russia), nominated at the National Centre for Radiation Research and Technology, Cairo, Egypt (dose rate 1.33KGy/h).

2.2 Synthesis procedure

Appropriate quantities of these components were dissolved in a minimum amount of water. This solution was mixed with the citric acid solution in a 1:1 volume ratio. A small quantity of nitric acid (1/5 the quantity of water) was also added to convert the corresponding precursors into their respective nitrates. The obtained solution was stirred at 70 °C and then the prepared solution was entered into the gamma irradiation cell at 25 kGy until it reached a gel-like consistency. The obtained gel was dried in an oven; the temperature was raised slowly to 250 °C and preserved overnight to produce a solid amorphous citrate precursor. The obtained powder was crushed, sieved, and calcined at 900 °C in the air for 6 h.

2.3 Characterizations

2.3.1 Structural and morphology

X-ray diffraction (XRD) patterns were acquired by utilizing XRD-6000 Shimadzu. X-ray diffractometer used CuKα radiation ($\lambda = 1.54059$ Å) in the range 2θ between (4 and 90°). The TGA analysis was executed using a Shimadzu

analyzer model TGA- 50 in the N_2 atmosphere at a heating rate of 10 °C/min up to 1000 °C. The morphological structure of the samples was deliberated using scanning electron microscopy (SEM) model JEOL-JSM5400, with an acceleration voltage of 30 kV. High-resolution transmission electron microscopy (HRTEM) images were acquired on a JEM-2010 microscope (Jeol, Akishima, Japan) (with an accelerating voltage of 200 kV and a resolution of 0.14 nm). The images were examined and filtered using the Digital Micrograph program (GATAN, Pleasanton, CA, USA). A suspension of perovskite particles in ethanol was deposited onto a copper grid support with an ultrasonic disperser. Fourier transform infrared spectroscopy (FTIR), BRUKER Vertex 70 optics layout, was used to depict the molecular structure and chemical bonds of $LaCo_{0.2}Mn_{0.8}O_3$ and La_2CoMnO_6.

2.3.2 Vibrational and intrinsic dielectric measurements

Raman scattering spectra were taken between 4 and $1200\ cm^{-1}$ at room temperature in a pseudo-back scattering configuration. Jobin–Yvon model U1000 double monochromator was utilized. The laser light source from a Spectra-Physics 2020 argon-ion laser is 514.5 nm line radiations. Each Raman scattering spectrum is the average of 12 consecutive scans acquired at a spectral resolution of $2\ cm^{-1}$. To realize the frequency stability and the accuracy of the apparatus, the Raman spectrum of silicon was recorded. Raman scattering spectra were recorded using a low excitation power of 10 mW, to avert sample photodecomposition or denaturation.

The 2 point-probe method was utilized to measure DC conductivity using a Keithley model 6517 A. The dielectric characterization dependence on frequency was done using an LCR meter (model 3532, HIOKI, Ueda, Nagano, Japan), with a capacitance measurement ~0.0001 pF and in a frequency region (50 Hz and 5 MHz).

2.3.3 Magnetic and ESR spectra measurements

The Vibrating Sample Magnetometer device Lake Shore 7410 was employed to check the magnetic properties. Magnetization hysteresis loop was collected at 300 K and up to 20 kOe. Temperature sweeps were collected between 100 and 300 K. ESR signal was measured at room temperature by an X-band EMX spectrometer (Bruker, Germany) using a standard rectangular cavity of ER 4102 to record the free radicals created in exciting material by the magnetic field. The operating parameters applied during the ESR experiment are microwave power (mW); modulation amplitude (Gauss); modulation frequency (at 100 kHz); sweep width (Gauss); microwave frequency (GHz); time constant (ms); conversion time (ms) and sweep time (s).
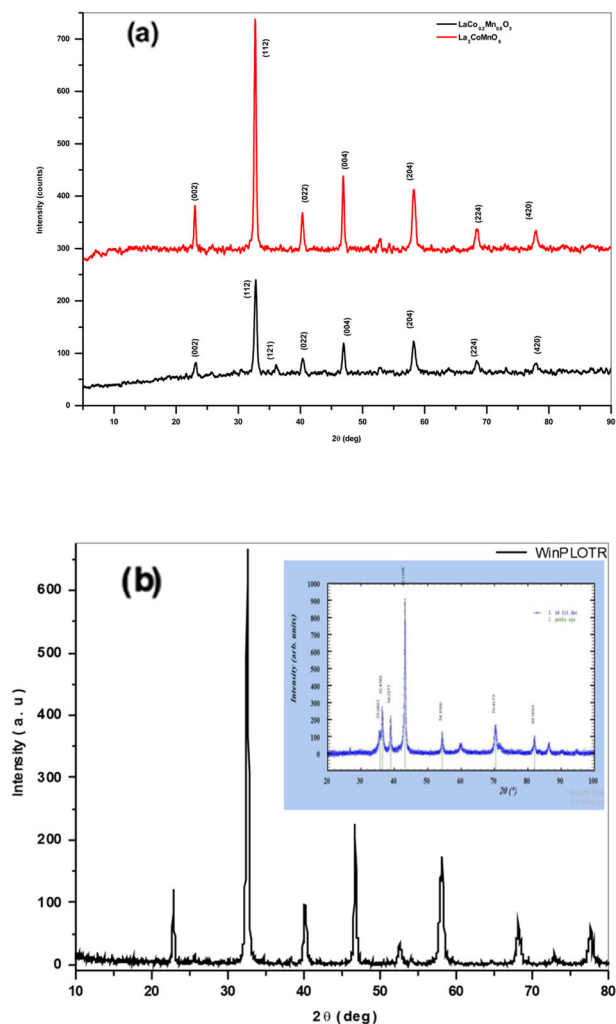

Fig. 1 a XRD pattern for $LaCo_{0.2}Mn_{0.8}O_3$ and La_2CoMnO_6 samples. **b** The x–y date and print-screen from image " Full-Prof program" for La_2CoMnO_6 Double Perovskite sample

3 Results and discussions

3.1 Structure and morphology studies

Room-temperature XRD measurements were executed over a 2θ range of 10–90° using a Cu-Kα source, as demonstrated in Fig. 1a for $LaCo_{0.2}Mn_{0.8}O_3$ and La_2CoMnO_6 samples. XRD patterns showed that the samples are quite crystalline without having any impurity phases. In additional meaning, have not extra reflection peaks than those of pure perovskite phase are detected. The crystal structure approved by La_2CoMnO_6 compound depends on cationic size, charge, and the ionic radii of rare earth, transition metal, and oxygen ratio, which are computed by tolerance factor [16]. With Matching to the tolerance factor, components of the double perovskite category have numerous structures, for instance: (i) cubic for $1.05 > t' > 1$, (ii) tetragonal for $1.00 > t' > 0.97$, and (iii) monoclinic/orthorhombic for $t' < 0.9$. The two
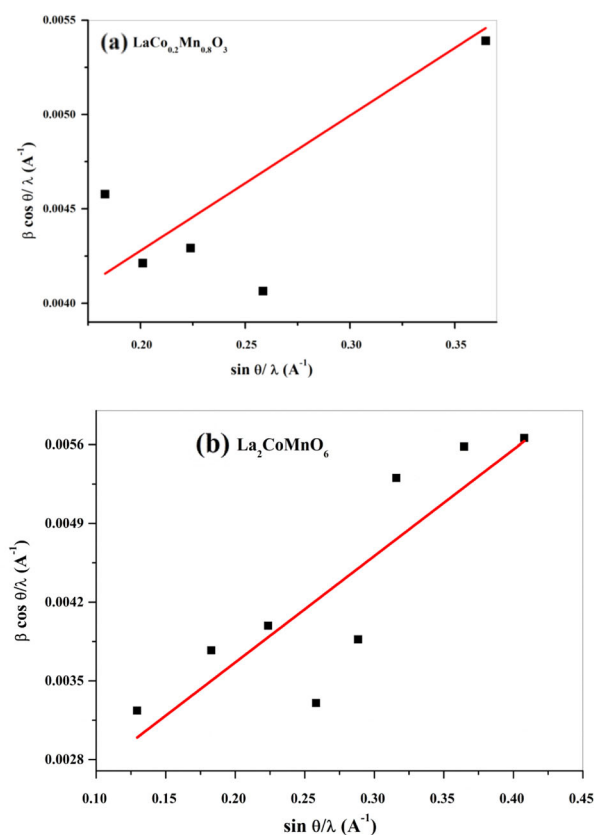
Fig. 2 The relation between $\beta \cos \theta/\lambda$ and $\sin \theta/\lambda$ for **a** $LaCo_{0.2}Mn_{0.8}O_3$ and **b** La_2CoMnO_6 samples

Table 1 The values of particle size and strain for the as-prepared samples

Sample	Particle size(nm)	Strain
$LaCo_{0.2}Mn_{0.8}O_3$	26.3	3.8×10^{-3}
La_2CoMnO_6	55.6	9.5×10^{-3}
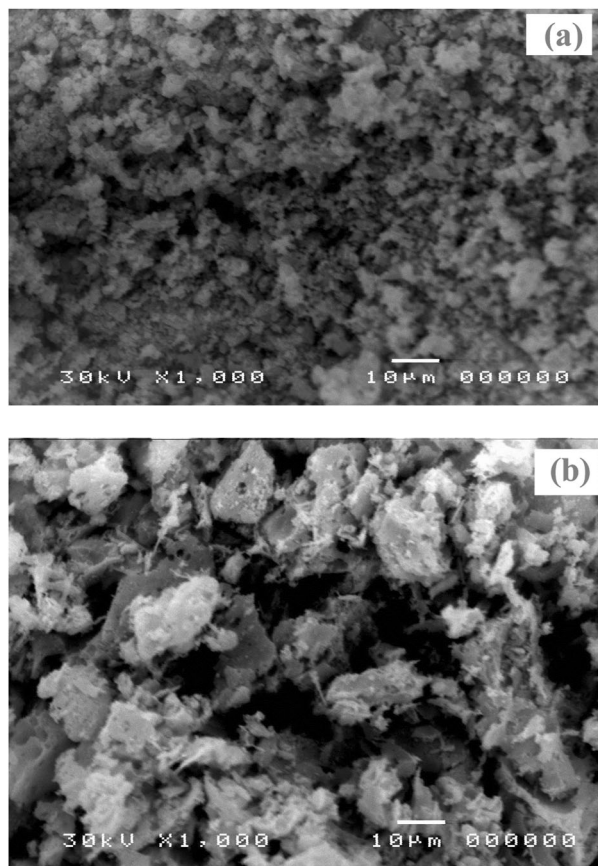
Fig. 3 SEM photographs of **a** $LaCo_{0.2}Mn_{0.8}O_3$ and **b** La_2CoMnO_6 samples

prepared samples were indexed according to the orthorhombic structure lattice that belongs to the space group Pb_{nm}, in agreement with ICSD no. 00-072-1186 by using the software "POWD MULT". Figure 1b the x–y date and print-screen from image "Full-Prof program" for La_2CoMnO_6 Double Perovskite sample. Also, we can calculate the crystallite size (D) and the microstrain (ε) of the samples using the Williamson-Hall (WH) analysis [17], in which these parameters are calculated using the following relation:

$$\mathbf{\beta \cos \theta/\lambda = k/D + 4\varepsilon \sin \theta/\lambda} \qquad (1)$$

where λ is the wavelength of incident radiation, k a dimensionless shape factor which assumes a typical value of ~0.9, and β the full width at half maximum (FWHM) of the diffraction peaks. Figure 2 represents β cos θ/λ vs. sin θ/λ plot for the checked samples. The amount of strain is given by the slope of the straight line. While the crystallite size is given by the intercept on the β cos θ/λ axis. Table 1 gives the obtained crystallite sizes (D) and microstrain (ε) values. The D values declare that the studied samples are nanometric. The considerable straight lines in the WH plotting signalize no dispersion in particle size and microstrain thus indicating that the samples display homogeneous particle size distributions and microstrain [18].

The morphology of the surface and particle distributions of the prepared samples was examined by SEM. The obtained photographs can be found in Fig. 3. From which it is obvious that the samples under study composed of multiple irregular flowers structure distributed in the less crystalline matrix. The photographs affirm that the particle aggregation became bigger and uniformly distributed for La_2CoMnO_6 sample. This signifies an increase in the crystalline character, and that sample is highly dense which confirms XRD results.

High-resolution TEM (HRTEM) can be used to demonstrate different morphologies and properties of different perovskite particles [19, 20]. The HRTEM images clearly showed orthorhombic phase with high crystallinity in the case of $LaCo_{0.2}Mn_{0.8}O_3$, while HRTEM La_2CoMnO_6

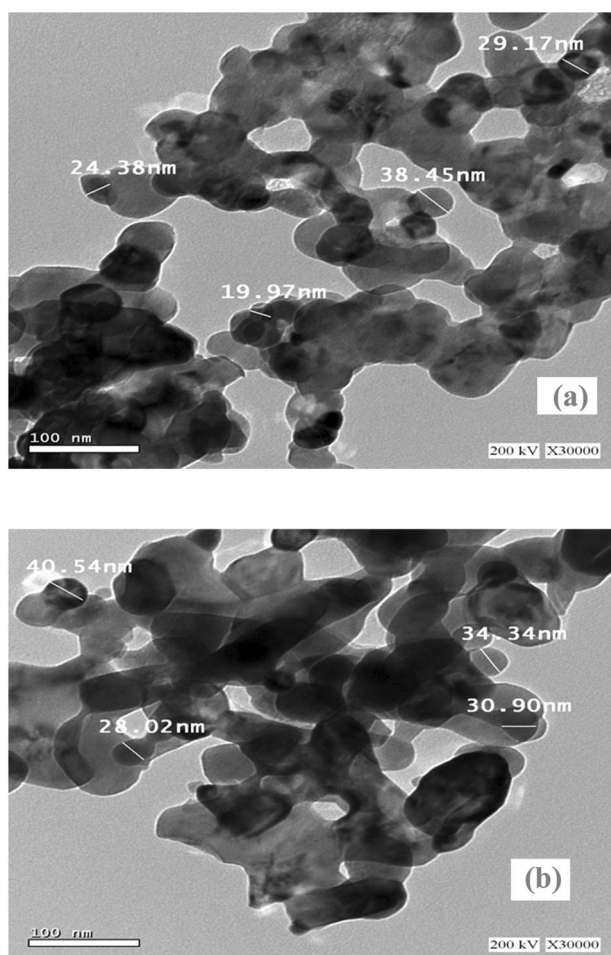Fig. 4 The HRTEM images of the as-prepared samples a $LaCo_{0.2}Mn_{0.8}O_3$, and b La_2CoMnO_6

Fig. 5 TGA and DTG thermograms of the as-prepared samples a $LaCo_{0.2}Mn_{0.8}O_3$, and b La_2CoMnO_6

showed hexagonal distorted rhombohedral phases. The phase purity of the as-prepared samples shows in Fig. 4; it shows that the samples mainly consist of well-crystallized, and no zones of amorphous phases were being found. The particle size of $LaCo_{0.2}Mn_{0.8}O_3$ is substantially smaller than in the case of La_2CoMnO_6. A full agreement between the particle sizes was investigated by HRTEM and the XRD data was observed.

3.2 Thermal decomposition

Figure 5 shows TGA and DTG thermograms of the synthesized LCMO nanoparticles. The figure illustrates that the decomposition process in the temperature extent from R.T. up to 1000 °C occurred in three weight loss regions. Thermal analysis can be used to determine thermal stability and decomposition prepared perovskite temperature. The optimum calcination temperature for perovskite can be determined using thermal analysis (TGA and DTG) of the citrate complex of (La, Co, and Mn) [19, 21, 22]. The TGA curve
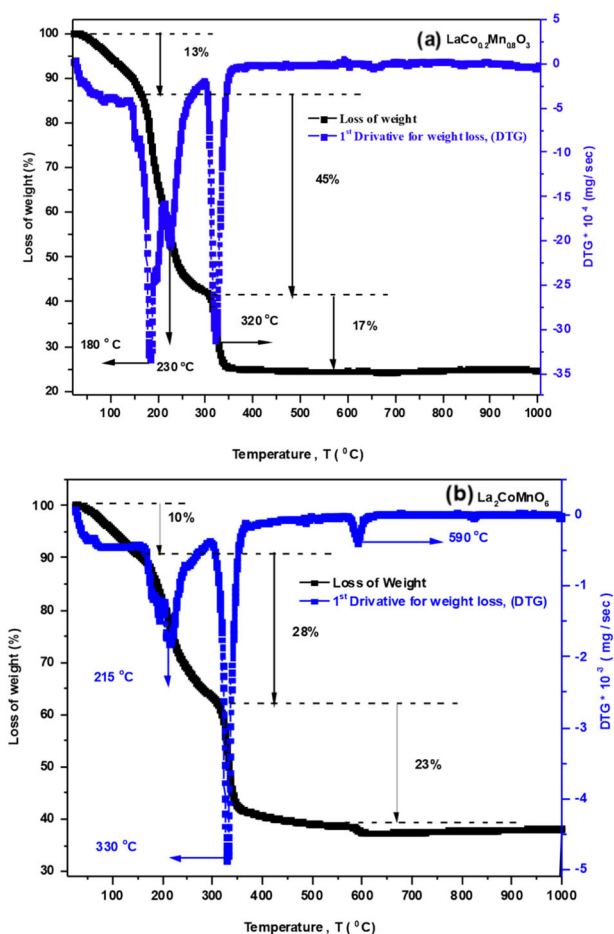
shows a weight loss of ~13, and 10% for $LaCo_{0.2}Mn_{0.8}O_3$, and La_2CoMnO_6 respectively, which due to the release of moisture absorbed in the sample. A Collapse (concurrent large weight loss) of the citrate complex could be ~45%, and 28% for $LaCo_{0.2}Mn_{0.8}O_3$, and La_2CoMnO_6 respectively, which due to the reaction of nitrates metals with citric acid has been occurred at a temperature of about 330 °C with a smooth weight loss step and sharp exothermic peak. La_2CoMnO_6 formation was achieved at ~590 °C through a small weight loss step [21] ~17%, and 23% for $LaCo_{0.2}Mn_{0.8}O_3$, and La_2CoMnO_6 respectively. Otherwise, there is no change in weight or enthalpy which occurs in the perovskite samples at temperatures as high as 800 °C. Also, the combustion is completed and no organic matter is present in the perovskite samples. So, there is no hard evidence phase transition occurs in the perovskite samples above 800 °C. Moreover, the completeness of nitrate → oxide thermal conversion with the help of a thermobalance with high resolution occurred up to 550 °C, which is performed in a closed furnace that controls the temperature and often allows inert gases N_2.
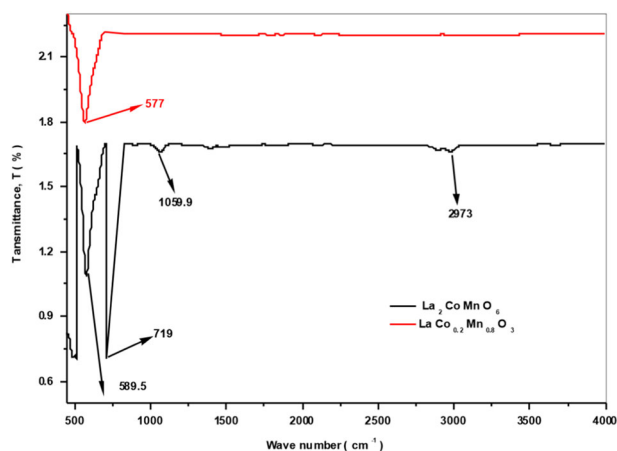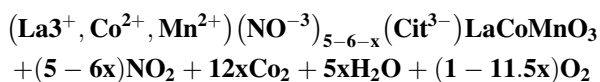
Fig. 6 FTIR spectra of $LaCo_{0.2}Mn_{0.8}O_3$, and La_2CoMnO_6 as-prepared sample

Fig. 7 Raman spectra of as-prepared LCMO samples

Due to the depletion of citric acid in the perovskite samples and the observed evolving gas ($NO_2 + CO_2$) during the second heat step. Thus, to explain both the apparent thermal characteristic of the second process and the observed emission of nitrogen dioxide, it is thought that the general reaction following the production of $LaCo_{0.2}Mn_{0.8}O_3$ occurs:

$$\left(La3^+, Co^{2+}, Mn^{2+}\right)\left(NO^{-3}\right)_{5-6-x}\left(Cit^{3-}\right)LaCoMnO_3$$
$$+(5-6x)NO_2 + 12xCo_2 + 5xH_2O + (1-11.5x)O_2$$

Note that from the above equation, there is no well-developed molecular oxygen, the determined ratio of citric acid/nitrate in the mixed compounds was 0.04, less than the theoretical value (0.27) computed for stoichiometric. Accordingly, the heat emission here is less than the expected stoichiometric reaction and thus limits completion of the direct reaction to perovskites materials.

3.3 Characteristics of bonding by FTIR

FTIR data for as-prepared samples are displayed in Fig. 6. The phase composition and purity of the prepared samples were described using the FTIR spectrum. We get the characteristic bonding, its vibration, and intensity from the amplitude of its absorbance. Normally, the main absorption band of the metal oxide bonds in the perovskite is in the range around 500–600 cm^{-1}, which the internal motion of a charge in Mn–O–Mn bond length in MnO_6 octahedral [23].

In $LaCo_{0.2}Mn_{0.8}O_3$, the concentrated absorption band observed at 577 cm^{-1} can be appointed to Mn–O stretching vibrations formed by the octahedral MnO_6 group. In La_2CoMnO_6, the band due to distorted stretching vibrations of $-CH_2$ groups can be observed at 2923 cm^{-1} [24]. The absorption peaks around 1059 cm^{-1} stands for the presence of carbonate [25]. The band 719 cm^{-1} is due to C–H bending [26]. The bands around 589.5 are distinctive
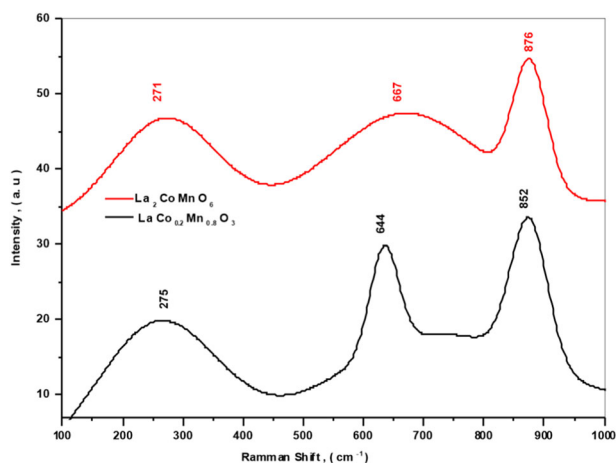
metal–oxygen bond internal phonon modes of MnO_6 octahedral. The stretching mode is associated with the change of Mn–O–Mn bond length and the bending mode incorporates the change of Mn–O–Mn bond angle. The feature of the stretching and bending modes at transmission spectra demonstrates that the perovskite structure of LCMO has been formed, which is convenient with the result of XRD.
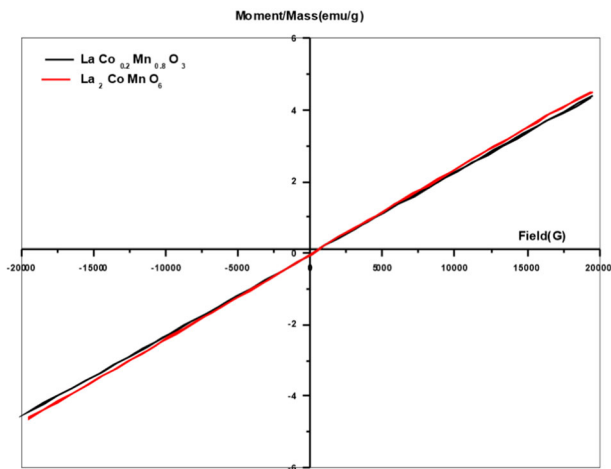
3.4 Raman spectroscopy

To know the local structure of different micro-phases or macro-phases presented in many manganites [26, 27], we can use Raman Spectroscopy. Figure 7 shows the room-temperature Raman spectra of as-prepared samples. It has been found that the spectra are essentially dominated by two broad peaks at 275.687 and 644.012 cm^{-1} for $LaCo_{0.2}Mn_{0.8}O_3$ sample, and 271.64 and 667.634 cm^{-1} for La_2CoMnO_6 sample, which can be appointed to antisymmetric stretching mode (or Jahn–Teller stretching mode, Ag) and symmetric stretching mode (Bg) of the (Co/Mn) O_6 octahedra, respectively, and are mightily related to lattice distortions, as well as the magnetic properties [28].

Moreover, we mention that the intensity of 644.012 cm^{-1} mode is higher and sharper in $LaCo_{0.2}Mn_{0.8}O_3$ sample than the intensity of 667.634 cm^{-1} in La_2CoMnO_6 sample; this is corresponding to X-ray data, where there is an increase in strain and distortion in the lattice for La_2CoMnO_6. It is appreciated that for the La_2CoMnO_6 compound, the lattice is structurally distorted in two ways: the MnO_6 and CoO_6 octahedral present a strong Jahn–Teller cooperative deformity due to Mn^{3+} and Co^{3+} ions, and the octahedral is tilted to optimize the La–O bond lengths. The maintenance of nonstoichiometric, including non-Jahn–Teller ions and Jahn–Teller ions, which can resemble the cation, associated defects, or oxygen, participated in the lattice distortions [29].

Table 2 The values of peaks position, FWHM, height, and area for as-prepared samples
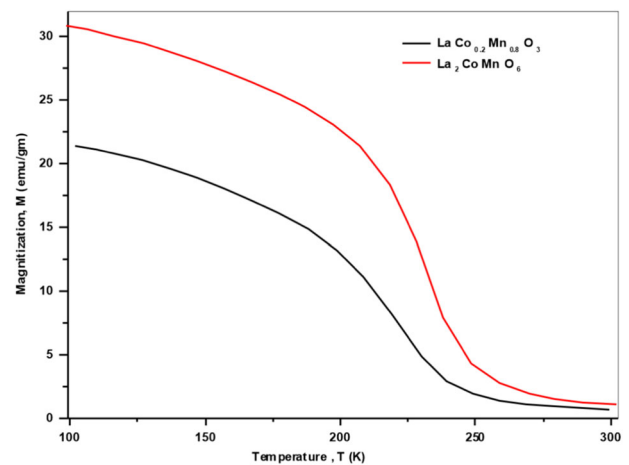
Samples	Peak position	Height	Area	FWHM
LaCo$_{0.2}$Mn$_{0.8}$O$_3$	275.687	12.4777	1816.29	136.747
	644.012	17.4545	2540.73	136.747
	852.403	20.2635	2949.62	136.747
La$_2$CoMnO$_6$	271.64	13.5149	2906.91	202.062
	667.634	12.9849	3946.83	285.546
	876.422	16.584	1149.58	65.1207

Fig. 8 The magnetization of the LCMO as-prepared samples at room temperature

Fig. 9 The variation of magnetization with the temperature at the applied magnetic field of 5000 Oe for the investigated samples

Table 3 The values of the magnetic transition temperature (T$_c$), the Curie–Weiss constant (C$_m$), the effective magnetic moment (μ_{eff}), and the molecular field constant (J)

Samples	T$_C$ (K)	C$_m$ (emu/mole)	μ_{eff}	J
LaCo$_{0.2}$Mn$_{0.8}$O$_3$	220	0.0096	0.2769	22916.7
La$_2$CoMnO$_6$	229	0.0146	0.3416	15684.9

As declared overhead, the entity of oxygen vacancies encouraged Mn^{3+} and Co^{3+} Jahn–Teller ions which increase the lattice distortion performing in the broadening of the Raman peaks and the decrease of peak intensity. The shifting of the position of the peak in two samples may take place, due to the surface strain of the crystal structure [30]. There are extra Raman modes at $852.403\,cm^{-1}$ for LaCo$_{0.2}$Mn$_{0.8}$O$_3$ sample, and $876.422\,cm^{-1}$ for the La$_2$CoMnO$_6$ sample which may be due to some distortion in the lattice or associated with stretching overtones. Table 2 shows the values of Peaks Position, FWHM, Height, and Area.

3.5 Magnetic properties

Figure 8 illustrates the magnetization data of the prepared nanoparticle samples at room temperature. The figure depicts a clear hysteresis with low coercivity and saturation magnetization at around 20 kOe. It is practically like a paramagnetic. At the very low field, it displays negligible loop like behavior, due to the spin exchanges. The moment (emu/g) resembles the previously reported values [31, 32]. The evidence of the inherent phenomenon is based on the careful analysis of the magnetism on the surface of the nano-structured magnetic grains.

The alteration of magnetization with the temperature for LCMO samples in the temperature extent 100–300 K at an applied field of 5 kOe is demonstrated in Fig. 9. The figure declares that the magnetization of field cooling (Fc) decreases as temperature increases. The obtained transition temperatures are shown in Table 3 for the as-prepared samples. The figure shows a clear single ferromagnetic (FM) transition temperature around T$_C \approx$ 220 K° for LaCo$_{0.2}$Mn$_{0.8}$O$_3$ and T$_C \approx$ 229 K° for La$_2$CoMno$_6$ samples. These achieved results declare that the magnetic phase transition temperature gradually broadens and shifts to lower temperatures as the grain size decreases. This indicates that the magnetic surface effect occurs in these grainy samples. Initial studies reveal that coupling among magnetic ions at the surfaces is much lower than that in the cores as a result of a massive number of hanging bonds and non-coordinating of atoms existing at the surface [33, 34].

In the prepared La$_2$CoMnO$_6$ nanoparticle sample, the distinctive magnetic transitions at different temperatures were remarked by the presence of various magnetic domains with different categories of exchange interactions, like Co^{3+}–O–Mn^{3+} and Co^{2+}–O–Mn^{4+} super-exchanges. In Co^{2+}–O–Mn^{4+} super-exchanges in abundantly ordered, are dependable for higher ferromagnetic ordering
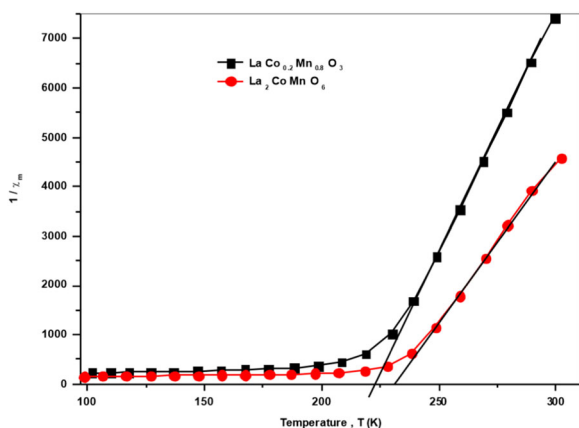
Fig. 10 The relation between temperature and magnetic susceptibility of LCMO samples in the region (100–300 K)

Fig. 11 The ESR spectra for LCMO nanoparticle samples

temperature (Tc ~229 K°) [35], while Co^{3+}–O–Mn^{3+} super-exchange interaction is responsible for the transition temperature [36]. Therefore, the variation of oxidations states of transition metal ions acts a vital role in their magnetic properties. It suggests that due to the substitution, the manifestation of the spin-glass state is suppressed. This fact is beyond reinforced by the ESR (electron spin resonance spectroscopy) will be studied.

Figure 10 shows the temperature reliance of magnetic susceptibility data of LCMO samples in the region (100–300 K). The decline was noticed in the 1/χ (T) curves and is explained by Griffiths phase (GP) [37, 38], which was initially recommended for randomly diluted Ising ferromagnets. This tendency of 1/χ (T) follows the general features of a GP phase where inverse susceptibility deviates from Curie–Weiss (CW) explanation at T → T$_c$. The Curie–Weiss law is specified by

$$\chi_m = C_m/(T - \theta) \tag{2}$$

with C$_m$ being the Curie–Weiss constant and θ the Curie–Weiss temperature.

For all samples, the positive value of θ = T$_c$ confirms a dominant FM interaction. The effective moment μ$_{eff}$ is linked to the Curie constant C$_m$ by the equation $C_m = (\mu_{eff})^2/2K_B$ where K_B is the Boltzman constant, hence it is probable to acquire it for the studied samples (Table 3).

3.6 ESR spectra

The electron spin resonance method is used for studying unpaired electrons or investigating oxygen-vacancy-related defects in materials. In ESR, electron spins are excited, but not the spins of atomic nuclei. Since the spin of the electron interacts with the magnetic field and spin is not been zero. Electron spin resonance (ESR) with frequency sweep and field sweep modes was used to record the coplanar
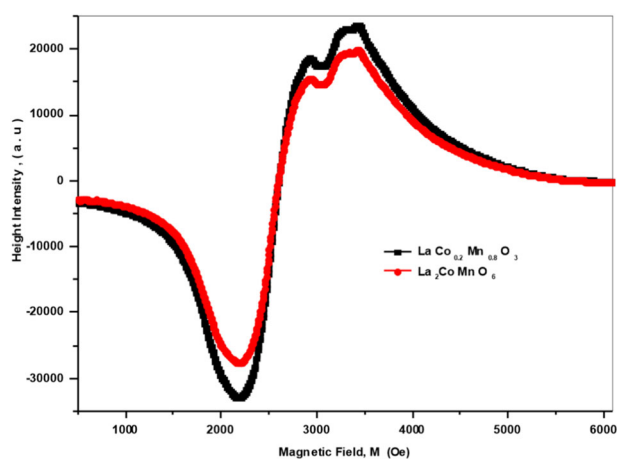
waveguide broadband spectrometer. Thus, we can obtain the spectroscopic splitting factor (g) to the material. ESR lines involve a superposition of two resonance modes, i.e., ferromagnetic and paramagnetic. Figure 11 shows the ESR spectra for LCMO nanoparticle samples. It has been found that the ferromagnetic resonance line has been seen in a smaller magnetic field. The ferromagnetic contribution may have occurred from the clusters of ferromagnetic ions in the samples. The larger linewidth is observed, due to the smaller degree of exchange restricting that can be expressed by Jahn–Teller ion behavior. Jahn–Teller of cobalt ions (Co^{+3}, Co^{+2}) were irregular distribution in the sample, becoming it hard to identify a pattern. In LaCo$_{0.2}$Mn$_{0.8}$O$_3$ the g-factor values g$_\parallel$ ~1.9047 and g⊥ ~1.997, while in La$_2$CoMno$_6$ only for this orbital 3d electron g$_\parallel$ ~2.00. ESR measurement will hint at the occurrence of Jahn–Teller glass comparable to the spin-glass behavior in the LCMO system, which has been ascribed as the semiconductor-to-metal transition. The role of La magnetism in La$_2$CoMno$_6$ is not noteworthy because of Co–Mn sublattice interacts weakly with the rare earth in double perovskites [39].

3.7 Dielectric measurements

The dielectric constant was obtained using the equation:

$$\varepsilon = C \cdot d/(\varepsilon_0 \cdot A) \tag{3}$$

Where C is the capacitance, d is the thickness, ε$_0$ is the permittivity of free space and A is the cross-section area of the pellet. Figure 12 shows the dielectric constant and loss dependence on frequency for LCMO samples. The dielectric constant decreases with increasing frequency, analogous to many of the dielectric materials.

At low frequency, the dielectric constant has a very high value because of the presence of numerous types of polarization (i.e. ionic, dipolar or orientation, electronic and space charge). While at high frequency the dielectric
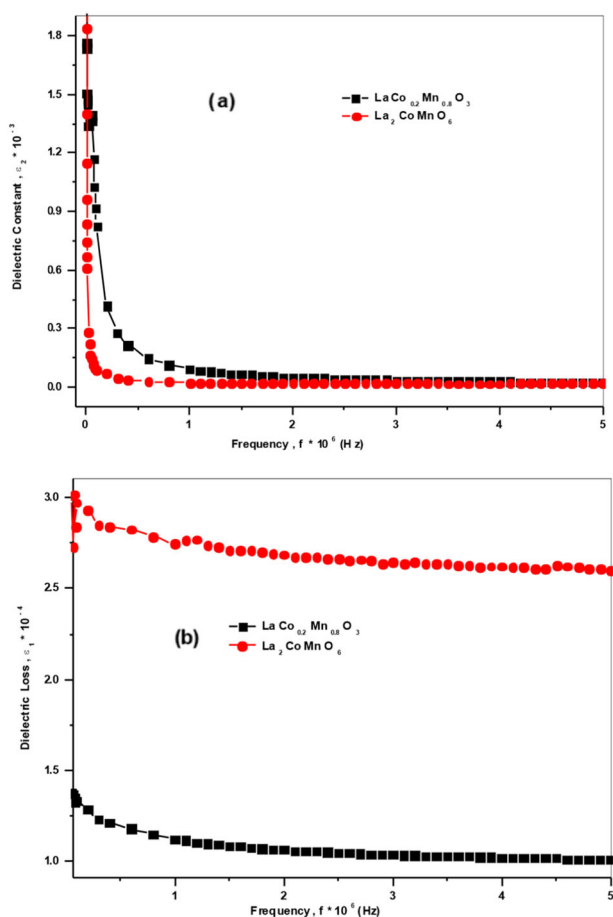
Fig. 13 The plot of imaginary electric modulus M'' and impedance Z'' as a function of frequency

Fig. 12 Frequency dependence on **a** The dielectric constant (ε_2) and **b** dielectric loss (ε_1) for the investigated samples at room temperature

constant was described by the main features of the polar dielectrics. The value of the dielectric constant will be small and polarons cannot be able to pursue the electric field at a higher frequency, which results in frequency-independent polarization [40–44].

At low frequency, the value of the dielectric loss is high because of the migration of ions in the material. But, at high-frequency, ion vibrations perhaps the only source of dielectric loss, and hence it has the minimum value. The distinctiveness of low dielectric constant and dielectric loss with frequency suggests that the samples possess reinforced optical quality with lesser defects and this parameter is of indispensable importance for various nonlinear optical materials and their applications [45]. As well-known as dielectric loss intends the extent of energy used by the applied field for the alignment of dipoles. So, the grains are particularly conducting as compared to the grain boundaries. In other words, at low-frequency, only the passage of charge carriers to the grain boundary produces a huge amount of energy loss.

According to Knoop's theory [46], the structure is implicated to consist of well-conducting grains separating by poorly conducting grain boundaries. The bulk and grain
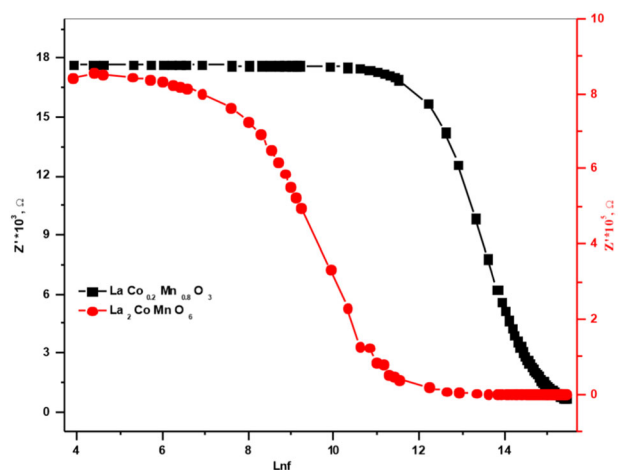
boundary assist in the total conductivity can be separated by using impedance measurement.

The high dielectric constant and relaxation property in LCMO prepared system was due to the local polarization from Mn^{4+} and Co^{2+} and extrinsic Maxwell–Wagner (M–W) polarization was advised to report for its irregular dielectric behavior [47]. On the other hand, the existence of internal boundary layers or external depletion layers creation at the interface of the sample/electrode was due to the Schottky barrier effect. For practical applications, the dielectric tunable materials have an essential high dielectric constant. So, the prepared LCMO nanoparticle system has gained a noteworthy interest because of potential applications of this type of electric tunable devices such as capacitors, phase shifters, microwave communication devices, filters, and oscillators [48, 49].

The impedance measurement as a function of frequency supplies the information about the real resistive part (Z') and imaginary or reactive part (Z'') of complex impedance. Figure 13 illustrates the variation of Z' as a function of frequency at R.T. This figure illustrates that the value of Z' has a high value at low frequency and decreasing with increasing frequency. The obtained Z' values of **LaCo$_{0.2}$Mn$_{0.8}$O$_3$** are found to be much smaller than those of **La$_2$CoMnO$_6$**.

The complex electric modulus (M*) of the material is used to study the bulk, grain boundary, electrode polarization, electrical conductivity, and relaxation process. The other benefit of a complex electric modulus is to overcome the electrode effect. Figure 14 shows that the plots of Z'' and M'' against frequency and displays a broad Debye peak. So, the complex electric modulus M* can be deemed using the following relation

$$\mathbf{M*} = \mathbf{M'} + \mathbf{jM''} \text{ where } \mathbf{M'} = \boldsymbol{\epsilon'} / \left(\boldsymbol{\epsilon'^2} + \boldsymbol{\epsilon''^2}\right) \text{ and } \mathbf{M''} = \boldsymbol{\epsilon''} / \left(\boldsymbol{\epsilon'^2} + \boldsymbol{\epsilon''^2}\right)$$

$$(4)$$
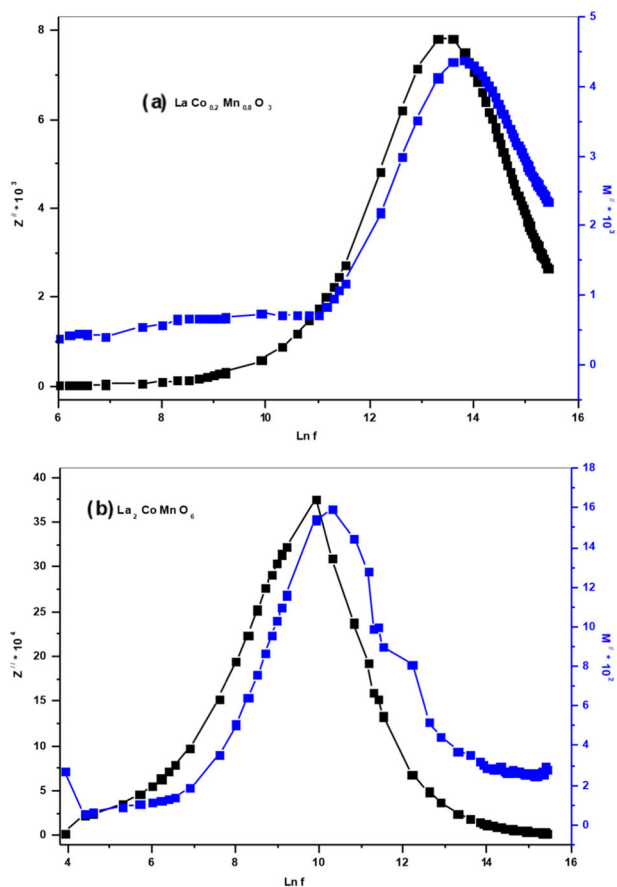
Fig. 14 Frequency dependence on real part (Z') for: **a** LaCo$_{0.2}$Mn$_{0.8}$O$_3$ and **b** La$_2$CoMnO$_6$

Fig. 15 The Nyquist plot of **a** LaCo$_{0.2}$Mn$_{0.8}$O$_3$, and **b** La$_2$CoMnO$_6$-samples at room temperature

The plot of imaginary electric modulus M$^{//}$ and impedance Z$''$ as a function of frequency is useful to reveal the effect of the smallest capacitance, the largest resistance and to recognize whether a relaxation process is due to short or long-range motion of charge carriers as proposed by Sinclair and West [50]. They reported that if the peaks in M$^{//}$ and Z$''$ against frequency occurred at the same frequency, the process is long-range and if the peaks occurred at different frequencies then the process is localized. In Fig. 13, we observed that with the increment of the frequency, the value of M$^{//}$ rises. Noticeably, we can be expected that at a frequency above 1 MHz the peak will shift to the right (high-frequency region), which is representative of the relaxation mechanism. The relaxation time is determined by the relation t (M$^{//}$) = 1/(2π f (M$^{//}$)), where f (M$^{//}$) is the frequency at which M$^{//}$ (ω) is maximum. The obtained values of t are 1.22 and 5.31 msec for LaCo$_{0.2}$Mn$_{0.8}$O$_3$ and La$_2$CoMnO$_6$, respectively.

The real (Z') and imaginary (Z$''$) component of the impedance are plotted as Nyquist or Cole–Cole plot. Hence, various relaxing components such as grain, grain boundary,
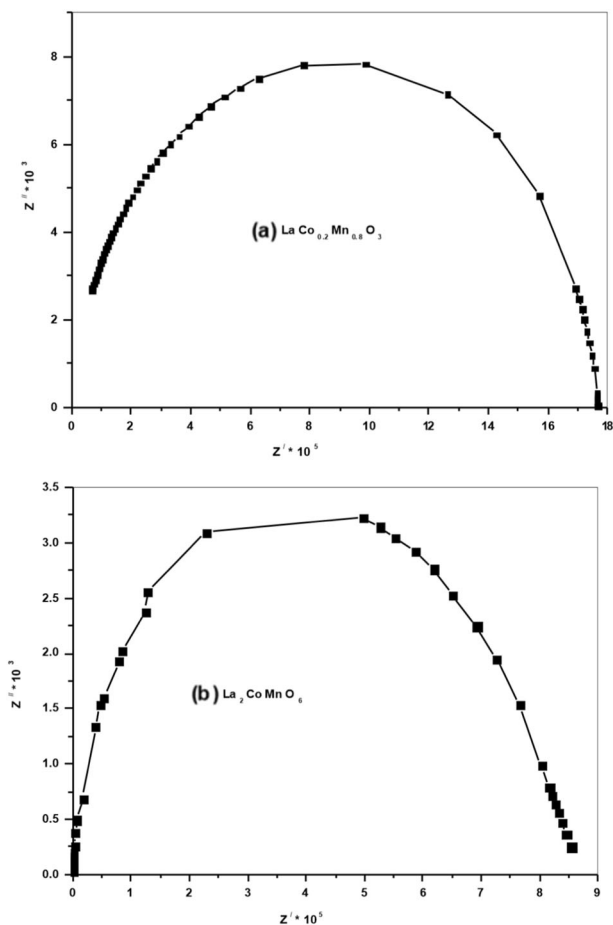
interface (due to space charge), and the electrode effect are explained by low-frequency, high-frequency, and intermediate-frequency-independent semicircles occurring sequentially. Each relaxing component displays a semicircle whose radius represents the resistance of the individual component. Figure 15 shows the Nyquist plot of LCMO samples at R.T. This figure shows a single semicircle, which occurs on account of a parallel combination of grain resistance (R$_g$) and grain capacitance (C$_g$). The apparition of a single semicircle means that the electrical process follows a single relaxation mechanism [51]. An increase in the radius of the semicircle is the representation of the increase in the resistance of LaCo$_{0.2}$Mn$_{0.8}$O$_3$ sample [52]. Figure 16 depicts the relation between real and imaginary electric modulus M$'$ and M$^{//}$ for LaCo$_{0.2}$Mn$_{0.8}$O$_3$ and La$_2$CoMnO$_6$ and equivalent circuit. An identical circuit of a series combination of resistances (R) and capacitances (C) is operated for an individual arc. A vanishing of an ideal Debye type of relaxation can be clarified by the CPE (constant phase element) which can be connected to the parallel RC system in the recommended circuit [53].
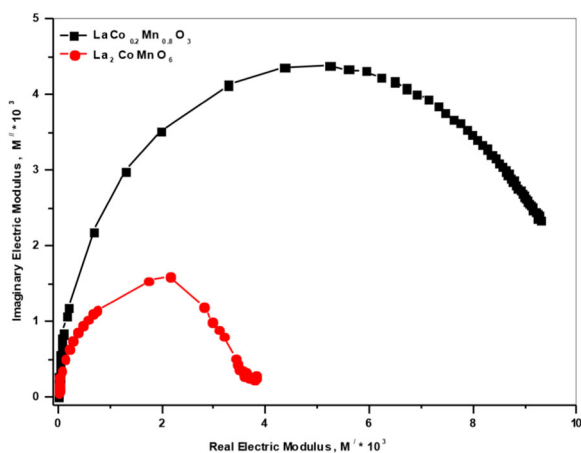
Fig. 16 The relation between real and imaginary electric modulus M' and M'' for $LaCo_{0.2}Mn_{0.8}O_3$ and La_2CoMnO_6

4 Conclusions

This study has reported the synthesis of $LaCo_{0.2}Mn_{0.8}O_3$ perovskites, and La_2CoMnO_6 double perovskites by the modified sol–gel route (citrate-gel method) with citric acid as the combustion agent. We have outright a detailed analysis of the action of cation nature in position B on the structural and magnetic characterization of the double perovskite. FTIR spectra and XRD patterns approved the perovskites phase formation for the samples under investigation. The investigated compounds are ferromagnetic and magnetic properties are indirectly affected by the distortion degree of the lattice and disorder on the B/B' positions. Further, this article has been studied the magnetic properties at low temperature from liquid nitrogen temperature to room temperature. These results suggest that these materials were orthorhombic structure lattice that belongs to the space group Pbnm (62), also there is a divergence between ZFC and FC in magnetization curves. Moreover, these materials have a high Tc single magnetic transition with a strong ferromagnetic (FM) super-exchange interaction between high-spin cations Co^{2+} and Mn^{4+}. The potential applications of these multifunctional materials were concluded conformist substances in solar cells, electric tunable devices, biomolecular, and gas sensing technologies. Long-range and Debye dielectric relaxation are imputed by electric modulus. The complex impedance spectra show the contribution of grains (bulk) only endorsed by the classical Cole–Cole plot. Especially in this article, the high dielectric tunability of these multifunctional materials has depicted an extraordinary concern of electric devices in these capacitors, phase shifters, microwave communication devices, filters, and oscillators.

Author contributions N.M. Yousif: conceptualization; data curation; formal analysis; funding acquisition; investigation; methodology; project administration; resources; software; visualization; validation; roles/writing—original draft; and review and editing. N. Makram: funding acquisition; resources; software; validation; writing—review and editing. L.A. Wahab: supervision.

Compliance with ethical standards

Conflict of interest We the undersigned declare that this manuscript is original, has not been published before, and is not currently being considered for publication elsewhere. We confirm that the manuscript has been read and approved by all named authors and that there are no other persons who satisfied the criteria for authorship but are not listed. We further confirm that the order of authors listed in the manuscript has been approved by all of us. We confirm that we have given due consideration to the protection of intellectual property associated with this work and that there are no impediments to publication, including the timing of publication, concerning intellectual property. In so doing we confirm that we have followed the regulations of our institutions concerning intellectual property. We understand that the Corresponding Author is the sole contact for the Editorial process (including Editorial Manager and direct communications with the office). I am responsible for communicating with the other authors about progress, submissions of revisions, and final approval of proofs.

Publisher's note Springer Nature remains neutral with regard to jurisdictional claims in published maps and institutional affiliations.

References

1. Gheorghiu F, Curecheriu L, Lisiecki I, Beaunier P, Feraru S, Palamaru MN, Musteata V, Lupu N, Mitoseriu L (2015) "Functional properties of Sm_2NiMnO_6 multiferroic ceramics prepared by spark plasma sintering". J Alloy Compd 649:151–158. https://doi.org/10.1016/j.jallcom.2015.07.136

2. Ramesh R, Spaldin NA (2007) Multiferroics: progress and prospects in thin films. Nat Mater 6:21–29. https://doi.org/10.1038/nmat1805

3. W Prellier, MP.Singh, P.Murugavel, the single-phase multiferroic oxides: from bulk to thin film, 2005, J. Phys. Condens. Matter. 17 R803 https://doi.org/10.1088/0953-8984/17/48/C01

4. Rogado NS, Li J, Sleight AW, Subramanian MA (2005) Magnetocapacitance and magnetoresistance near room temperature in a ferromagnetic semiconductor: La_2NiMnO_6, Adv. Mater 17:2225–2227. https://doi.org/10.1002/adma.200500737

5. Tiwari RM, Gadhvi M, Nag A, Vasanthacharya NY, Gopalakrishnan J (2010) Manganese-mediated ferromagnetism in $La_2Fe_{1-x}Mn_{2x}Cr_{1-x}O_6$ perovskite oxides. J Chem Sci 122:529–538. https://doi.org/10.1007/s12039-010-0087-7

6. Dimitrovska-Lazova S, Aleksovska S, Tzvetkov P (2015) Synthesis and crystal structure determination of $YCo_{1-x}Fe_xO_3$ (x = 0, 0.33, 0.5, 0.67 and 1) perovskites. J Chem Sci 127:1173–1181. https://doi.org/10.1007/s12039-015-0878-y

7. Dass RI, B J (2003) Goodenough, Multiple magnetic phases of $La_2CoMnO_{6-\delta}$ ($0 \le \delta \ge .05$). Phys Rev B 67:014401. https://doi.org/10.1103/PhysRevB.67.014401

8. Feng C, Ruan S, Li J, Zou B, Luo J, Chen W, Dong W, Wu F (2011) Ethanol sensing properties of $LaCo_xFe_{1-x}O_3$ nanoparticles: effects of calcination temperature, Co-doping, and carbon nanotube-treatment. Sens Actuators B Chem 155:232–238. https://doi.org/10.1016/j.snb.2010.11.053

9. Bin F, Song C, Lv G, Song J, Gong C, Huang Q (2011) $La_{1-x}K_xCoO_3$ and $LaCo_{1-y}Fe_yO_3$ perovskite oxides: preparation, characterization, and catalytic performance in the simultaneous removal of NO_x and diesel soot. Ind Eng Chem Res 50:6660–6667. https://doi.org/10.1021/ie200196r

10. Vulchev V, Vassilev L, Harizanova S, Khristov M, Zhecheva E, Stoyanova R (2012) Improving of the thermoelectric efficiency of $LaCoO_3$ by double substitution with nickel and iron. J Phys Chem C 116:13507–13515. https://doi.org/10.1021/jp3021408

11. Popa M, Hong LVA, Kakihana M (2003) Nanopowders of $LaMeO_3$ perovskites obtained by a solution-based ceramic processing technique. Phys B Condens Matter 327:233–236. https://doi.org/10.1016/S0921-4526(02)01736-2

12. Park JH, Cheong SW, Chen CT (1997) Double-exchange ferromagnetism in La $(Mn_{1-x}Co_x)O_3$. Phys Rev B55:11072. https://doi.org/10.1103/PhysRevB.55.11072

13. Iliev MN, Gospodinov MM, Singh MP, Meen J, Truong KD, Fournier P, Jandl S (2009) Growth, magnetic properties, and Raman scattering of La_2NiMnO_6 single crystals. J Appl Phys 106:023515. https://doi.org/10.1063/1.3176945

14. Singh MP, Truong KD, Jandl S, Fournier P (2010) Multiferroic double perovskites: opportunities, issues, and challenges. J Appl Phys 107:09D917. https://doi.org/10.1063/1.3362922

15. Merino NA, Barbero BP, Ruiz P, Cadús LE (2006) Synthesis, characterization, catalytic activity and structural stability of $LaCo_{1-y}Fe_yO_{3\pm\lambda}$ perovskite catalysts for combustion of ethanol and propane. J Catal 240(2):245–257. https://doi.org/10.1016/j.jcat.2006.03.020

16. Shannon RD (1976) Revised effective ionic radii and systematic studies of interatomic distances in halides and chalcogenides. Acta Crystallogr A 32:751–767. https://doi.org/10.1107/S0567739476001551

17. Williamson GK, Hall WH (1953) X-ray line broadening from filed aluminum and wolfram. Acta Metall 1:22–33. https://doi.org/10.1016/0001-6160(53)90006-6

18. Gonçalves NS, Carvalho JA, Lima ZM, Sasaki JM (2012) Size–strain study of NiO nanoparticles by X-ray powder diffraction line broadening. Mater Lett 72:36–38. https://doi.org/10.1016/j.matlet.2011.12.046

19. Vijayakumar C, Kumar HP, Solomon S, Thomas JK, Warrier PRS, Koshy J (2008) Synthesis characterization, sintering and dielectric properties of nanostructured perovskite-type oxide, Ba_2GdSbO_6, Bulletin. Mater Sci 31(5):719–722. https://doi.org/10.1007/s12034-008-0113-2

20. Ali SM, Abd Al-Rahman YM, Galal A (2012) Catalytic activity toward oxygen evolution of $LaFeO_3$ prepared by the microwave-assisted citrate method. J Electrochem Soc 159(9):F600–F605. https://doi.org/10.1149/2.063209jes

21. Galal A, Atta NF, Darwish SA, Abd El Fatah AA, Ali SM (2010) Electrocatalytic evolution of hydrogen on a novel $SrPdO_3$ perovskite electrode. J Power Sources 195:3806–3809. https://doi.org/10.1016/j.jpowsour.2009.12.091

22. Ghosh S, Dasgupta S (2010) Synthesis, characterization, and properties of nanocrystalline perovskite cathode materials. Mater Sci—Pol 28(2):427–438. http://cgcri.csircentral.net/id/eprint/740

23. Gao F, Lewis RA, Wang XL, Dou SX (2002) Far-infrared reflection and transmission of $La_{1-x}Ca_xMnO_3$. J Alloy Compd 347:314–318. https://doi.org/10.1016/S0925-8388(02)00789-2

24. Annapoorani S, Parameswaran VR (1999) Studies on Complexes of 1,2-Bis-(8-quinoxy) Ethane with Some Bivalent Metal Ions. Asian J Chem 11:763–766

25. Boo BH (2011) Infrared, and Raman Spectroscopy of Diphenylsilane. Vibrational Assignment by Hartree-Fock and Density-functional Theory Calculations. J Korean Phys Soc 59:3205–3209. https://doi.org/10.3938/jkps.59.3205

26. Zhao S, Shi L, Zhou S, Zhao J, Yang H, Guo Y (2009) Size-dependent magnetic properties, and Raman spectra of La_2NiMnO_6 nanoparticles. J Appl Phys 106:123901. https://doi.org/10.1063/1.3269707

27. Iliev MN, Guo H, Gupta A (2007) Raman spectroscopy evidence of strong spin-phonon coupling in epitaxial thin films of the double perovskite La_2NiMnO_6. Appl Phys Lett 90:151914. https://doi.org/10.1063/1.2721142

28. Liu WJ, Shi L, Zhou S, Zhao J, Y LI, Guo Y (2014) Griffiths phase, spin-phonon coupling, and exchange bias effect in double perovskite Pr_2CoMnO_6. J Appl Phys 116:193901. https://doi.org/10.1063/1.4902078

29. Iliev MN, Abrashev MV, Litvinchuk AP, Hadjiev VG, Guo H, Gupta A (2007) Raman spectroscopy of ordered double perovskite La_2CoMnO_6 thin films. Phys Rev B 75:104118. https://doi.org/10.1103/PhysRevB.75.104118

30. Iliev MN, Abrashev MV, Popov VN, Hadjiev VG (2003) Role of Jahn-Teller disorder in Raman scattering of mixed-valence manganites. Phys Rev B 67:212301. https://doi.org/10.1103/PhysRevB.67.212301

31. Guo H, Burgess J, Street S, Gupta A (2006) Growth of epitaxial thin films of the ordered double perovskite La_2NiMnO_6 on different substrates. Appl Phys Lett 89:022509. https://doi.org/10.1063/1.2221894

32. Huang HY, Cheong SW, Ong NP, Batlogg B (1996) Spin-polarized intergrain tunneling in $La_{2/3}Sr_{1/3}MnO_3$. Phys Rev Lett 77:2041. https://doi.org/10.1103/PhysRevLett.77.2041

33. Trajanovic Z, Kwon C, Robson MC, Kim KC, Rajaswari M, Lofland SE, Bhagat SM, ForkR D, Venkatesan R,T (1996) Growth of colossal magnetoresistance thin films on silicon. Appl Phys Lett 69:1005. https://doi.org/10.1063/1.117967

34. Sattler K, Miihlbach J, Recknagel E (1980) Generation of metal clusters containing from 2 to 500 Atoms. Phys Rev Lett 45:821. https://doi.org/10.1103/PhysRevLett.45.821

35. Cowen JA, Stolzman B, Averback RSA, Han H (1987) Magnetic phase transitions in nanocrystalline erbium. J Appl Phys 61:3317. https://doi.org/10.1063/1.338894

36. Dass RI, Goodenough JB (2003) Multiple magnetic phases of $La_2CoMnO_{6-\delta}$ ($0\leq\delta \geq 0.05$). Phys Rev B 67:014401. https://doi.org/10.1103/PhysRevB.67.014401

37. Blasco J, García J, Subías G, Sánchez MC (2004) Structure and magnetic properties of $LaMn_{1-x}Mg_xO_3$ compounds. Phys Rev B 70:094426. https://doi.org/10.1103/PhysRevB.70.094426

38. Salamon MB, Chun SH (2003) Griffiths singularities and magnetoresistive manganites. Phys Rev B 68:014411. https://doi.org/10.1103/PhysRevB.68.014411

39. Salamon MB, Lin P, Chun SH (2002) Colossal Magnetoresistance is a Griffiths singularity. Phys Rev Lett 88:197203. https://doi.org/10.1103/PhysRevLett.88.197203

40. Booth RJ, Fillman R, Whitaker H, Nag A, Tiwari RM, Rama nujachary KV, Gopalakrishnan J, Lofland SE (2009) An investigation of structural, magnetic and dielectric properties of R_2NiMnO_6 (R = rare earth, Y). Mater Res Bull 44(7):1559–1564. https://doi.org/10.1016/j.materresbull.2009.02.003. ISSN0025-5408

41. Huang T, Chang Y, Chen G, Chung C, Chang Y (2007) J. Electrochem. Soc 154:244–250

42. Acharya S, Chakrabarti PK (2010) Some interesting observations on the magnetic and electric properties Al^{3+} of doped lanthanum

orthoferrite ($La_{0.5}Al_{0.5}FeO_3$) Solid State Commun., 150:1234. https://doi.org/10.1016/j.ssc.2010.04.006

43. Jawahar K, Choudhary RNP (2008) Structural and dielectric properties of $LaBi_2Fe_5O_{12}$. Indian J Eng Mater Sci 15:203–206. http://nopr.niscair.res.in/handle/123456789/1974

44. Haron W, Thaweechai T, Wattanathana W, Laobuthee A, Manaspiya H, Veranitisagul C, Koonsaeng N (2013) Structural characteristics and dielectric properties of $La_{1-x}Co_xFeO_3$ and $LaFe_{1-x}Co_xO_3$ synthesized via metal-organic complexes. Energy Procedi 34:791–800. https://doi.org/10.1016/j.egypro.2013.06.815

45. Rajarajan K, Mani G, Potheher IV, Jesudurai JGM, Vimalan M, Christy D, Madhavan J, Sagayarai P (2007) Growth, optical, dielectric and ESR studies on tetrathiourea mercury(II) tetra-thiocyanato manganate(II): an organometallic complex NLO crystal. J Phys Chem Solids 68:2370–2375. https://doi.org/10.1016/j.jpcs.2007.07.036

46. Koops CG (1951) On the dispersion of resistivity and dielectric constant of some semiconductors at audio frequencies. Phys Rev 121:83. https://doi.org/10.1103/PhysRev.83.121

47. Chandrasekhar KD, DAS AK, Mitra C, Venimadhav A (2012) The extrinsic origin of the magnetodielectric effect in the double perovskite La_2NiMnO_6. J Phys Condens Matter 24:495901. https://doi.org/10.1088/0953-8984/24/49/495901

48. Kleemann W, Dec J, Wang R, Itoh M (2003) Nonlinear susceptibility, and phase transition in $SrTi^{18}O_3$. Phys Rev B 67:092107. https://doi.org/10.1103/PhysRevB.67.092107

49. Liang X, Wu W, Meng Z (2003) Dielectric, and tunable characteristics of barium strontium titanate modified with Al_2O_3 addition. Mater Sci Eng B 99:366–369. https://doi.org/10.1016/S0921-5107(02)00461-0

50. Shukla A, Choudhary NP, Thakur AK (2009) Thermal, structural and complex impedance analysis of Mn^{4+} modified $BaTiO_3$ electroceramic. J Phys Chem Solid 70:1401–1407. https://doi.org/10.1016/j.jpcs.2009.08.015

51. Snclair DC, West AR (1989) Impedance and modulus spectroscopy of semiconducting $BaTiO_3$ showing positive temperature coefficient of resistance. J Appl Phys 66:3850. https://doi.org/10.1063/1.344049

52. Jyothy PV, ArunKummar KV, Karthiska A, Rajesh R, Unnikrishnan NV (2010) Dielectric and AC conductivity studies of CdSe nanocrystals doped sol-gel silica matrices. J Alloy Comp 493:223–226. https://doi.org/10.1016/j.jallcom.2009.12.060

53. Sahoo S, Mahapatra PK, Choudhary RNP (2016) "The structural, electrical and magnetoelectric properties of soft chemically-synthesized $SmFeO_3$ ceramics". J Phys D Appl Phys 49:035302. https://doi.org/10.1088/0022-3727/49/3/035302